Doped tungsten oxide microstructures for enhancing ultraviolet sensing based on ZnO/glass transparent acoustic wave technology

Hui Ling Ong,[1] Yihao Guo,[2] Kunyapat Thummavichai,[1,*] Jian Zhou,[2] Jikai Zhang,[1] Luke Haworth,[1] Yunhong Jiang,[3] Meng Zhang,[3] Zabih Ghassemlooy,[1] Qiang Wu,[1] Yong-Qing Fu,[1,*]

[1] Faculty of Engineering and Environment, Northumbria University, Newcastle upon Tyne, NE1 8ST, UK

[2] College of Mechanical and Vehicle Engineering, Hunan University, Changsha 410082, China

[3] Hub of Biotechnology in the Building Environment, Department of Applied Science, Northumbria University, Newcastle upon Tyne, NE1 8ST, UK

*Corresponding authors:

Dr. Kunyapat Thummavichai, email: kunyapat.thummavichai@northumbria.ac.uk;

Prof. Richard Yongqing Fu, email: Richard.fu@northumbria.ac.uk

Abstract: Metal element (Nb, Er, and Gd) doped WO_x powders were prepared via a one-step solvothermal method to enhance photocatalytic property of WO_x, and they were used to enhance ultraviolet (UV) sensing performance of ZnO/glass surface acoustic wave (SAW) devices. Results showed that Gd-doped WO_x has a better photocatalytic performance amongst the other doped WO_x (Nb and Er), which can be explained using the different reductions of band gaps after doping. Gd-doped WO_x coated on the ZnO/glass SAW device demonstrates the best performance in enhancement of UV sensitivity which is 14 times higher than the uncoated SAW device. The incorporation of dopants Gd into the WO_x matrix leads to a multitude of effects that collectively enhance the UV sensing performance, including modified band gap, increased charge carrier generation, enhanced conductivity, efficient charge separation, and recombination suppression. Electrical properties and UV sensing mechanisms on ZnO/glass SAW devices based on Gd-doped WO_x were studied, and the frequency shifts in these SAW devices are primarily due to ultraviolet-induced changes in conductivity and thermal effects.

Keywords: Surface acoustic wave; rare-earth metal; tungsten oxide; ultraviolet; sensing; ZnO.

1. Introduction

Solar irradiation constitutes a key source of ultraviolet (UV) radiation, characterized by photons of high energy and short wavelengths in the solar spectrum [1]. UV sources are classified into four regions based on wavelength, including UV-A (315- 400 nm), UV-B (285-320 nm), UV-C (200- 280 nm), and vacuum-UV or far UV (10- 200 nm) [2]–[5]. The UV-A and UV-B bands (3.1- 4.43 eV), which can penetrate the air and pose direct harm to human health [5], [6], have been the subject of extensive research. UV light irradiation has been documented to induce material degradation and accelerates corrosion processes [3], [7]. One common example is the degradation of solar panels with glass or polymer layer, which can negatively impact their performance, durability, and guaranteed module lifetime [1], [4], [8], [9]. Therefore, there have been numerous studies aimed to develop UV sensors for monitoring UV radiations.

Various types of UV sensors have been actively developed (e.g., photochromic and photoelectric UV sensors) due to their various applications such as astronomical research, environmental studies, and medical applications [5], [10]–[12]. Photochromic UV sensors utilize the photochromic properties of molecules, which change color in response to changes in UV intensity [5]. However, the quantification of color changes or detection of signals often requires the usage of a spectrophotometer [5]. In contrast, photoelectric UV sensors convert UV radiation into electrical signals through the absorption of UV photons using the semiconducting materials [5]. These sensors utilize the bandgap energy of the semiconducting materials to generate photocurrents through the creation of electron hole (e^-/h^+) pairs after absorption of UV photons [5]. Various studies have showed that materials such as silicon and gallium nitride (GaN) can be used as an absorbing layer in most of these UV detectors [10], [13], [14]. However, these materials often have issues such as degradation in transparency or reduced efficiency [15]. To circumvent these issues, SAW-based UV sensors have received significant attention due to their unique advantages, including wireless operation, low power consumption, high sensitivity, ease of fabrication, and reasonably good stability and reproducibility [16]–[19]. Changes in resonant frequency of the SAW device can be induced by the changes in acoustic wave velocity due to UV light illuminations with varying intensities and durations [20]–[22].

Enhancement of UV sensing capabilities can be achieved through the incorporation of a UV-sensitive layer onto surface acoustic wave (SAW) devices. Among the commonly used metal oxides for UV sensing technologies, zinc oxide (ZnO) and titanium dioxide (TiO_2) have been extensively studied due to their easy fabrication and the potential for engineering different morphologies and optical properties [23]–[25]. With a bandgap energy of 3.37 eV and a large exciton binding energy of 60 meV at room temperature, ZnO has demonstrated exceptional performance in UV sensing applications [5], [26]–[28]. Another metal oxide which has also received significant attention in the field of UV sensing is tungsten oxide (WO_x). With better mechanical, chemical, and thermal stabilities compared to other metal oxides such as ZnO, WO_x has shown high work functions ranging from 5.2-6.4 eV, exhibiting a higher visible light transparency, and possessing a higher electron mobility [29]–[33]. Furthermore, its bandgap and other properties are easily tuned through stoichiometric and crystallographic modifications, making it a promising candidate for use as a sensitive layer for UV sensors [34]–[36].

Utilization of doping or mixing with other elements or metal oxides is one of the key methods of band gap engineering in the context of UV sensing. By reducing the band gap through this approach, an increase in the grain size or lattice distortion of the WO_x matrix and creation of impurity levels below the conduction band of WO_x can be achieved [37]–[39]. Its optical bandgap can be altered, thereby making it capable of sensing in the UV and visible regions [32], [40]. Studies have reported the doping of WO_x with lanthanide-based materials or rare earth elements such as cerium (Ce), terbium (Tb), and lanthanum (La) as well as transition metals such as niobium (Nb) has improved the photocatalytic activities [41]–[44]. When the 4f orbital of rare earth metals is not completely occupied and the 5d orbital is empty, electrons are captured efficiently and recombination rate of photo-generated charge carriers can also be reduced [41], [44]. This will allow the electrons to be captured efficiently and the recombination rates of photo-generated charge carriers to be reduced [41]. Furthermore, the increase in the amount of oxygen vacancies on the surface of the photocatalytic materials results in an enhancement in photocatalytic activity [32], [41], [44]. Various studies have shown the advantages of erbium and gadolinium doped WO_x such as excellent optical response, wide spectral range from high energy photons (X-ray) to radiation considered transparent biological window (750 to 950 nm), instantaneous responses, and high sensitivity [45]–[47]. On the other hand, doping WO_3 with Nb (a transition metal) leads to improvements in its optical-electrochemical properties, as it does not cause large lattice mismatching strains due to

the similar ion radius of W (0.62 Å) and Nb (0.69 Å) [42]. Additionally, doping with Nb creates defect states and provides active sites for ion redox reactions on the surface of the WO_3, further enhancing its optical-electrochemical properties [42]. Despite these potential benefits, there is limited research available on the application of doped WO_x in SAW-based UV sensing.

In this paper, we proposed the doping of WO_x with Nb, Er, and Gd elements and investigated effects of various doped WO_x layers on the UV sensing performance of ZnO/glass SAW devices. The focus of this paper is to elucidate the underlying mechanisms of UV-induced changes in frequency shifts, which are commonly induced by thermal effects and changes in UV conductivity. Gd-doped WO_x has shown the best performance amongst the other two doped WO_x. This can be explained using the differences in the reductions of band gaps after doping which result in the different enhancement in their photocatalytic performance.

2. Experimental details

2.1. Materials

The chemicals used in this study were acquired from Merck and were used as received without any further purification or treatment. These chemicals include tungsten hexachloride (WCl_6), niobium (V) chloride anhydrous ($NbCl_5 \cdot 7H_2O$), gadolinium (III) chloride hydrate ($GdCl_3 \cdot 6H_2O$), erbium (III) chloride hexahydrate ($ErCl_3 \cdot 6H_2O$), and cyclohexanol. All chemicals had a trace metals basis of 99.995% for $NbCl_5 \cdot 7H_2O$, 99.99% for $GdCl_3 \cdot 6H_2O$, and 99.9% for $ErCl_3 \cdot 6H_2O$.

2.2 Preparation doped WO_x samples

Preparation of pure WO_x, and Nb-, Gd-, and Er-doped WO_x powder samples was achieved through a one-step solvothermal method [29]. Tungsten hexachloride (WCl_6) and cyclohexanol were utilized as the main precursor and organic solvent, respectively. The preparation process began with the dissolution of WCl_6 (0.1189 g) into 60 ml of cyclohexanol, forming a solution with a molarity of 0.005 M. This solution was then transferred into a Teflon-lined stainless-steel autoclave and subjected to a reaction at 200°C for 10 hours.

For the preparation of the doped samples, $NbCl_5 \cdot 7H_2O$, $GdCl_3 \cdot 6H_2O$, and $ErCl_3 \cdot 6H_2O$ were dissolved in either ethanol or distilled water (depending on the solubility of the precursor) to form a pre-solution. This pre-solution (1 ml) was added into a 59 ml WCl_6-cyclohexanol solution and mixed through ultra-sonication for 30 minutes. The resulting homogeneous

solution was then transferred to the Teflon-lined stainless-steel autoclave and reacted at 200°C for 10 hours. The molar ratio of the dopants ($NbCl_5 \cdot 7H_2O$, $GdCl_3 \cdot 6H_2O$, or $ErCl_3 \cdot 6H_2O$) to WCl_6 was 1:4. Upon completion of the reaction, the autoclave was naturally cooled down in an oven. The obtained samples were then washed three times with distilled water, ethanol, and acetone, before being collected through centrifugation at 8000 rpm for 10 minutes. The samples were then dried at room temperature in a fume hood for two days and were ready for further characterization and testing. **Figure S1** in the supporting information illustrates the preparation and characterization processes of the doped WO_x powders, which was then further used for UV sensing.

2.3 Characterisation of doped WO_x powders

Morphologies and microstructures of the WO_x-based samples were characterized using a scanning electron microscope (SEM, Tescan Mira 3). Energy dispersive X-ray spectroscopy (EDX, Oxford Instruments) was employed to analyse the elemental composition of the powders. Crystallinity of the samples was studied utilizing X-ray diffraction (XRD, D5000, Siemens, Cu-Kα radiation, 40 kV, 30 mA), utilizing a Cu Kα radiation source (λ = 0.15406 nm) operated at 2 kW. The XRD analysis was performed using a Rigaku SmartLab SE. The band gap of the WO_x-based samples was determined through the analysis of their ultraviolet and visible (UV-Vis) absorption spectra, which were recorded using a diffuse-reflectance spectrophotometer (UV-Vis, Shimadzu 2450). The samples were prepared by mixing 0.04 g of WOx-based material with 4 ml of ethanol and ultrasonically agitated for 60 minutes to form a uniform colloidal solution. The solution was then coated onto a standard glass slide using a spin coater at a spin speed of ~800 rpm. The thickness of the resulting thin film was measured using a Dektak Stylus profilometer. Given that WO_x is an indirect-bandgap semiconductor, the band gap (E_g) was calculated using Eq1 :[30]

$$(h\nu\alpha)^{1/n} = A(h\nu - E_g) \quad (1)$$

where h, n, a, E_g and A are the Planck's constant, frequency of vibration, the absorption coefficient, the band gap, and a proportional constant, respectively. With $n = 2$ being used in the calculations, due to the indirect nature of the bandgap of WO_x [30].

2.4 ZnO/glass SAW device fabrication and characterisation

Deposition of ZnO thin films onto a four-inch glass wafer was performed utilizing a direct current (DC) magnetron sputter (NS3750, Nordiko), utilising a zinc target with a purity of 99.99%. During the film deposition process, the substrate was positioned with a distance 20 cm away from the target, and the surface of the Zn target was oxidized and sputtered after the introduction of argon and oxygen gases with an Ar/O_2 flow ratio of 10/15 SCCM. The plasma power was set at 400 Watts, while the vacuum pressure in the chamber was carefully controlled to maintain at ~0.35 Pa.

The interdigital transducers (IDTs) were patterned on the surface of the ZnO thin film through a conventional photolithography and lift-off process. Subsequently, a bilayer of Cr/Au was desposited on the IDTs, with thicknesses of 20 nm/100 nm, as the electrodes using a thermal evaporator (Edwards AUTO306). The IDTs were designed with a wavelength of 16 μm, comprising of 30 pairs of electrodes. **Figure S2** illustrates the SAW sensor fabrication process of the ZnO/glass SAW device, which was used as an UV sensor. The reflection spectra (S11) of the SAW devices were measured using a network analyser (Keysight, FieldFox N9913A). The resonant frequency (f_o) of the SAW devices was determined to be 162.58 MHz. The temperature coefficient of frequency (*TCF*) for the SAW devices was also obtained, which represents the rate of change in the resonant frequency with temperature, using the following Eq. 2 [48], [49]:

$$TCF = \frac{1}{f_0}\frac{df}{dT}\ (ppm/K) \quad (2)$$

The *TCF* of ZnO/glass SAW devices was measured by monitoring their resonant frequencies while the devices were heated from 20 to 60 ℃ in a controlled environment using a laboratory oven (Carbolite^{TM} LHT).

2.5 UV Sensing using WO_x powders

To prepare sensitive layers for UV sensing, pure WO_x and Nb-, Gd- and Er- doped WO_x powders were mixed separately with ethanol (0.04 g in 4 ml) to form a uniform solution under ultrasonic agitation for 60 mins. Subsequently, each mixture solution was drop-casted onto the IDTs of the ZnO/glass SAW device with a volume of 2 microliters, and then dried in an oven at 80 ^oC for an hour. The UV sensing tests were performed using a UV light source with varied power densities (with a maximum value of 89.5 mV/cm^2) at the wavelength of 365 nm

(CS2010, Thorlabs), which was positioned approximately 5 mm above the surface of the SAW device. The frequency responses of the SAW device were recorded at different UV light intensities, with measurements obtained by switching the UV light for 5s. The sensitivity (*S)* of the UV intensity was calculated using the Eq. 3 [18]:

$$S = \frac{\Delta f}{\Delta I_{UV}\, f_0} \tag{3}$$

where Δf is the change in frequency of the SAW device, ΔI_{UV} is the change of the intensity of the UV source illuminate on the sensing layer and f_o is the resonant frequency.

To gain an understanding of the frequency shifts induced by changes of electrical conductivity, the surface conductivity of the ZnO thin film was characterized by measuring the current-voltage (I-V) characteristics. This was accomplished using a Keithley 2400 source meter, whit probes connected to the IDT pads. The current was recorded by sweeping the voltage from -0.5 to 5V, with a compliance of 0.1 A, using a LabVIEW program to capture the current and voltages values. To assess the surface heating effects during UV illumination at varied intensities, an infrared (IR) camera (FLIR, T620bx) was utilized to monitor the temperature changes on the surface of the SAW devices as the temperature was increased.

3. Results and discussion

3.1. Characterisation of powders and film

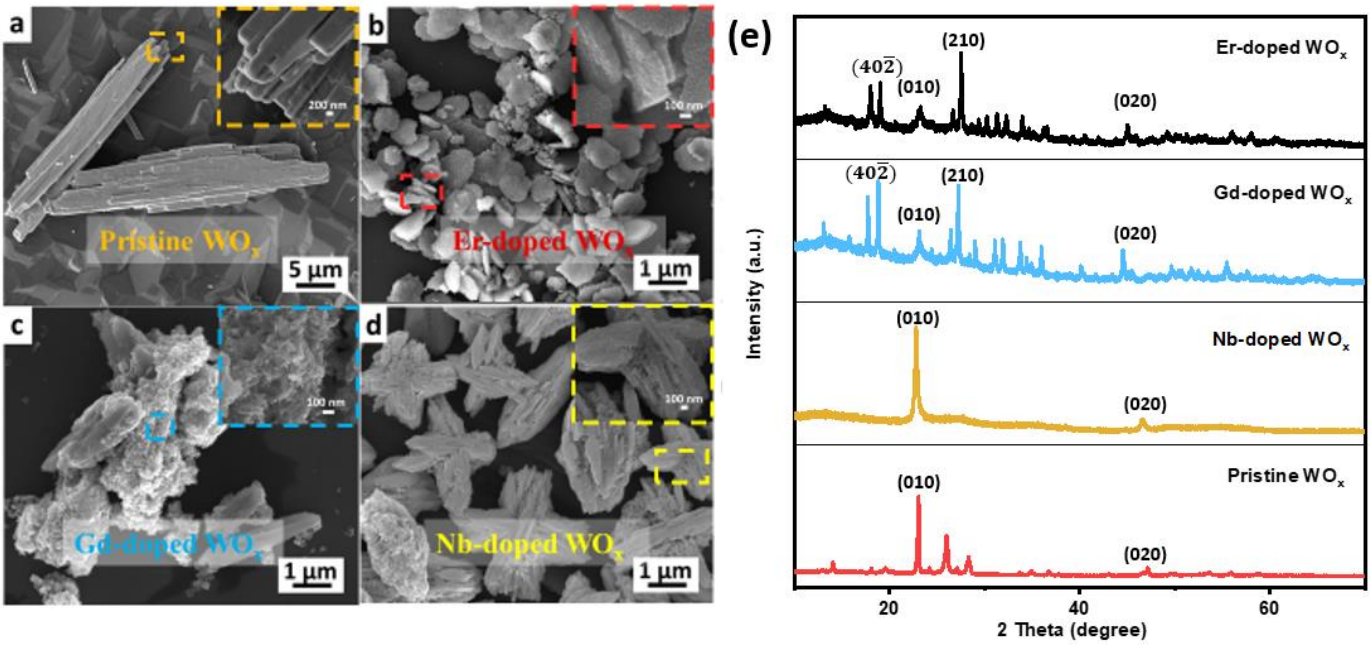

Figure 1: SEM images of the powders of (a) pure WO_x, (b) Nb-doped WO_x, (c) Gd-doped WO_x, (d) Nb-doped WO_x. The inset images in each panel provide a high-magnifacation view of each sample, (e) shows the XRD patterns of powders of pure WO_x, as well as Nb-, Gd- and Er-doped WO_x.

Morphology of the pure WO_x powder was characterized by SEM and the image is shown in **Figure 1a.** The images show stack of rod-like structures with lengths in the range of 25-35 µm and heights of 5 µm. A high-magnification image, shown in the inset of **Figure 1a,** reveals that the rod-like structures are composed of small lamina held together along their long axis. For the Er-doped WO_x samples, disk-like morphologies with diameters ranging from 500 nm to 2 µm were observed, as shown in **Figure 1b**. The discs are comprised of small rod-like structures with lengths in range of 100-200 nm. The Gd-doped WO_x powder samples are composed of agglomerated nanorods with diameters of 10-20 nm and lengths of approximately 100 nm, as shown in **Figure 1c**. The Nb-droped WO_x samples show flower-like structures with diameters of 3-4 µm and a heights of 2-3 µm , as shown in **Figure 1d**.

Figures S3a to S3d in the supporting information show the obtained SEM elemental mapping of pure WO_x, as well as Nb-, Gd- and Er-doped WO_x. The presence of both oxygen and tungsten elements can be observed in the EDS spectrum in **Figure S3a**, suggesting that the two elements are present in the pristine WO_x powder sample (**Figure 3a)**. From **Figure S3b**, presence of erbium, oxygen, and tungsten is observed in the EDS spectrum, suggesting that these three elements are present in the Er-doped WO_x. Similarly, presence of gadolinium and niobium is observed along with oxygen and tungsten in the EDS spectrum from **S3c and S3d**, respectively, which further suggests that these elements are present in both the Gd- and Nb-doped WO_x powder samples.

The obtained XRD patterns of the various doped WO_x powders are shown in **Figure 3e**. The diffraction peaks are in accordance with those of monoclinic $W_{18}O_{49}$ (called m-$W_{18}O_{49}$, JCPDS 00-153-8315). The obtained dominant peaks at $2\theta = 23.12°$ and 47.17° are corresponding to planes of (010) and (020), respectively, of the pristine WO_x. The obtained peaks are consistent with those of JCPDS 00-153-8315, which has the dominant peaks at 23.45° and 47.96° corresponding to planes (010) and (020), respectively [41]. Upon doping with rare-earth metals of Er, Gd, and transition metal Nb, there are slight shifts in the peak positions of the WO_3 monoclinic phase. For example, for the (010) peak, the peak shifts are 23.57°, 24.35°, and 23.2° for the Er, Ga, and Nb doped WO_x, respectively. Addtion to this, both Er and Gd have $(40\bar{2})$

peak at 19.81° and 19.86°, respectively, which are consistent with JCPDS 00-152-8166 and 00-153-8315 for Er and Gd, respectively. Based on the obtained doped-WO_x diffractograms, the Nb-doped WO_x exhibits a pattern which is similar with that of the pristine WO_x. The slight peak shift observed the Nb-doped WO_x could be atttributed to the lattice enlargement as the size of Nb is larger than W (i.e., 0.69 Å versus 0.6 Å). As for both Er- and Gd-doped WO_x, the peak shifts are much larger, which could be due to the larger ionic radii of Er and Gd than W (i.e., 1 Å and 1.8 Å, respectively, versus 0.6 Å). Consequently, it has been reported that the presence of the dopant elements located in the interstitial site of lattice structures results in significant stress due to the dissimilarity in ionic radii between the rare earth metals and tungsten [41]. The Scherrer formula was used to calculate and estimate the crystallite size using the Debye-Scherrer formula expressed as follows [50], [51].

$$D = \frac{k\,l}{\beta_D \cos\theta} \tag{4}$$

where λ, K, β_D, and θ denote the incident X-ray wavelength, shape factor, full width at half maximum (FWHM), and diffraction angle, respectively. It should be noted that the decrease in crystallite size is beneficial for the transfer of photo-generated charge-carriers to the surface of photocatalyst as it allows the enhancement in photocatalytic performance via the reduction of charge-carriers recombination rate [41]. The crystallite sizes were estimated to be 26.94 µm, 1.80 µm, 18.06 nm, and 3.20 µm for WO_x, Er-doped WO_x, Gd-doped WO_x, and Nb-doped WO_x respectively, which are in good agreements with those obtained from SEM analysis.

The d-spacing, dislocation density (δ), and micro-strain (ε) were also calculated using Eqs. (5), (6), and (7) [50]–[52].

$$\lambda = 2d\,sin\theta \tag{5}$$

$$\delta = D^{-2} \tag{6}$$

$$\varepsilon = \frac{\beta_D}{4\,\tan\theta} \tag{7}$$

Following the utilised equations, the otbained d-spacing values are decreased upon doping with different elements, implying that the dopants are much more densely packed with WO_x, resulting in a more densitified crystalline structure. The dislocation densities of the doped WO_x are increased when compared to pure pristine WO_x, and this implies the introduction of cystallographic defects in the microstructure of the materials could act as active sites for the enhancement in UV sensitivity. The microstrain values of Er- and Gd- doped WO_x were

observed to increase after doping, which may be arised from inhomogeneous variations of crystal lattices. This in turn can result to an increment in charge carrier generation, which is related closely to the non-radiative recombination loss [53].

Table 1: D-spacing, dislocation density, and micro-strain values of the WO_x and doped WO_x

	d-spacing	Dislocation density (δ)	Micro-strain (ε)
WO_x	3.84 Å	1.37×10^{-3} $(\mu m)^{-2}$	6.39×10^{-2}
Er-doped WO_x	3.77 Å	0.308 $(\mu m)^{-2}$	0.1045
Gd-doped WO_x	3.65 Å	3.06×10^{-3} $(\mu m)^{-2}$	0.1011
Nb-doped WO_x	3.83 Å	0.0976 $(\mu m)^{-2}$	6.37×10^{-2}

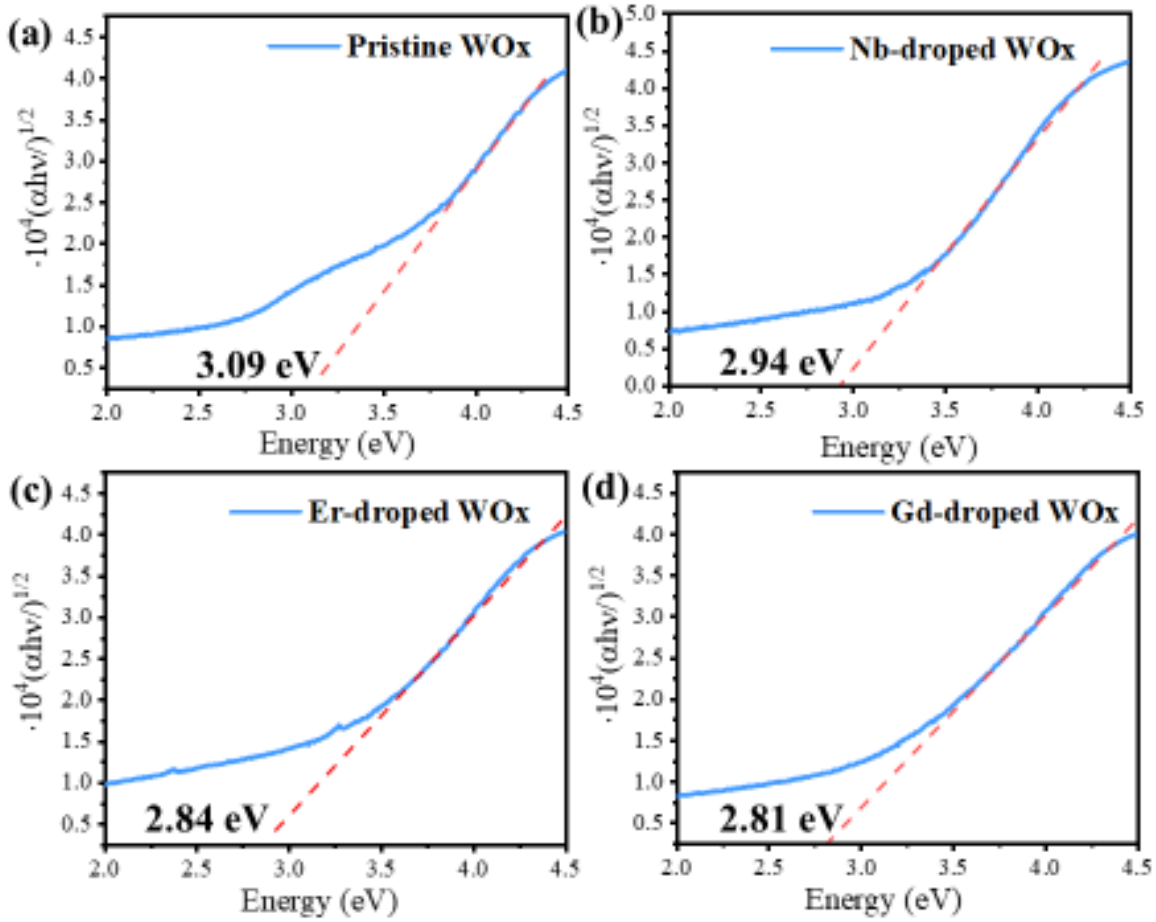

Figure 2: Band-gap (E_g) of UV-Vis Absorption Spectra Using Tauc Plot (a) WO_x, (b) Nb-doped WO_x, and (c) Er-doped WO_x, (d) Gd-doped WO_x

The UV-Vis absorption spectra for powders of pristine WO_x, and their Nb-, Er- and Gd-doped counterparts are presented in **Figure 2**. The band-gap values were obtained using the Eq. 1 and the data from the Tauc plots, which were found to be 3.09 eV, 2.94 eV, 2.84 eV, and 2.81 eV, respectively. The results reveal a decrease in the band gap of WO_x upon doped with Nb, Er, or Gd elements. The mechanism behind the effect of ion doping on the band gap of WO_x is complex and influenced by a number of factors, including the size and distribution of the dopant ions, the nature of the chemical bonds formed between the dopant and the WO_x lattice, and the crystal structure of the WO_x material. Nb, Er, and Gd are belonged to the group of transition and rare-earth metals, and their ionic radii are easily changed according to their oxidation states. Nb typically displays an ionic radius of 0.63 Å in its +5 oxidation state, whereas Er and Gd exhibit ionic radii of 0.86 Å and 1.1 Å, respectively, in its +3 oxidation state [41]. The size of the dopant ions has a direct effect on the band gap of WO_x. A larger ion size results in the

lattice expansion and increased distortions, which can lead to a decrease in the band gap. The size of the Gd ions is larger than those of Nb and Er ions, and thus doping results in a larger lattice distortion, ultimately leading to a much reduced band gap [41]. Moreover, the unique 4f electrons of Gd element alters the electron energy band structure of WOx [41]. Thus, the large atomic radius of Gd significantly affects lattice structures and changes energy band structure of WOx, leading to a reduction in the band gap after doping [41].

We have previously reported the microstructure and crystalline properties of a ZnO film deposited on the glass substrate [48]. The results indicated the presence of a vertically columnar ZnO structure with a thickness of 4.17 microns, revealing a preferred (0002) orientation [48]. The deposition of the ZnO film resulted in a transparency level greater than 70% for the glass substrate [48], which could potentially be enhanced through post-anneaing processes. The electro-mehcanical coupling coefficeint (k^2) of the SAW device was calcualted using Eq. 8:

$$k^2 = \frac{\pi}{4N}\left(\frac{G}{B}\right)_{f=f_0} \tag{8}$$

where N is the finger pairs of the IDTs, G and B are the radiation conductance and susceptance of the input port at the resonant frequency obtained from the Smith chart of the network analyser, respectively [48], [54]. The obtained k^2 value is 0.85% [48]. The TCF value of the SAW device was ~ -76 ppm/ ^{o}C, similar to those reported in Ref. [48], [55].

3.2. UV acousitc wave sensing results with different WOx layers.

Figure 3a presents the freqeuncy shifts of the ZnO/glass SAW device upon a single cycle of UV swtiching on and switching off, with varied UV light intensities ranging from 0% to 100%. The results demonstrate that upon activation of the UV light, the frequency of the SAW device experiences a significant decrease, before reaching a stable value. Upon deactication of the UV light, the frequency quickly returns to its orginal data.There may be residual freqeuncy shifts, which may be attributed to lingering UV heating effects.

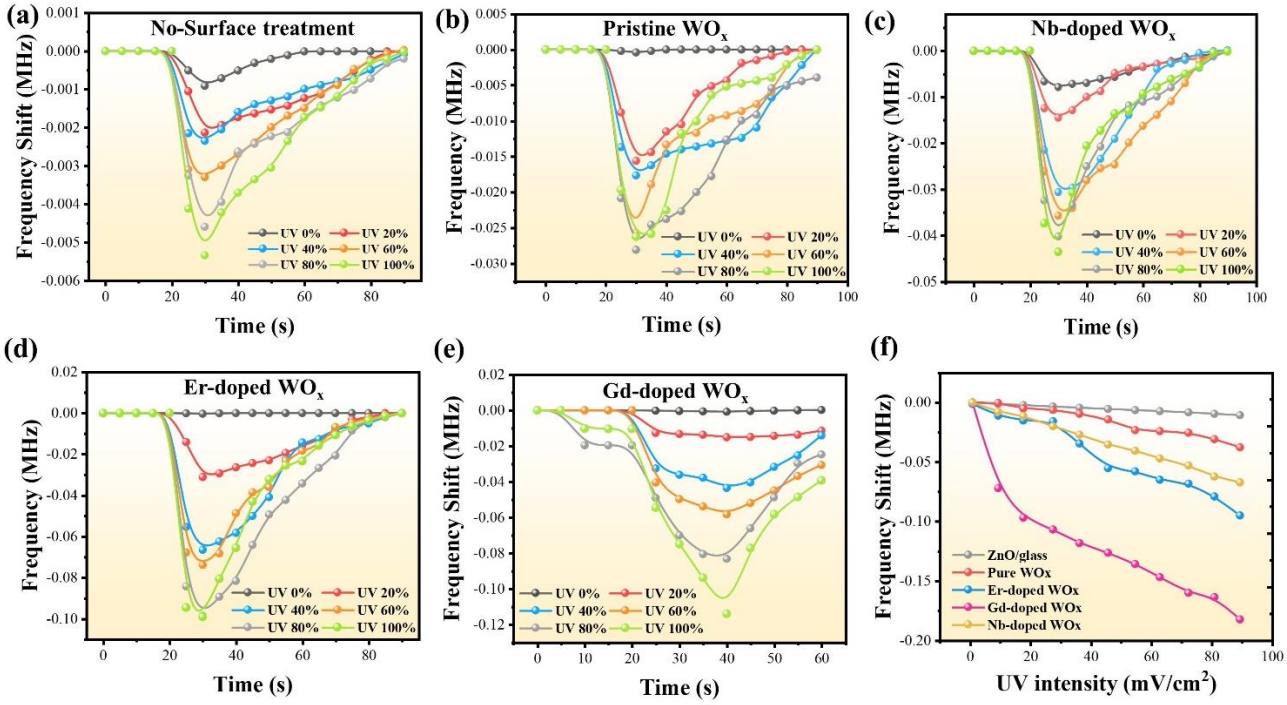

3__

Figure 3: (a) Frequency shifts in response to various UV light intensities of ZnO/glass SAW device; Frequency shifts in response to various UV light intensities with a sensing layer of (b) Pure WO_x, (c) Nb-doped WO_x, (d) Er-doped WO_x, (e) Gd-doped WO_x, (f) UV sensing results of ZnO/glass SAW device, ZnO/glass SAW device with sensing layers of pure WO_x, Er-doped WO_x, Gd-doped WO_x, and Nb-doped WO_x from 0.756 to 89.5 mV/cm^2

As depicted in **Figure 3b**, the resonance frequency of the device, incorporating pristine WO_x, experiences a considerable decline upon exposure to UV light. In comparison to the untreated device (**Figure 3a**), the magnitude of this decrease is ~5 times higher. This sensitivity arises from the presence of oxygen vacancies and defects in the crystal structure of WO_x, which act as trap states for electrons. When UV light is absorbed by the WO_x material, it causes an excitation of electrons from the valence band to the conduction band, leading to a change in the conductivity of the material.

Figures 3c to **3e** present the ultraviolet (UV) spectral properties of WO_x samples doped with Nb, Er, and Gd ions, respectively. The results demonstrate that the sensitivity, sensing limit, and maximum frequency shift of the WO_x samples with dopants are greater than those of the undoped counterpart. This is primarily attributed to the reduction of the bandgap energy as a result of the doping process. The reduction in bandgap energy reduces the energy required for

electrons to be transferred from the valence to the conduction band, thus rendering the material more susceptible to UV excitation. This conclusion is consistent with the results shown in **Figure 2**.

The cycling responses to UV light intensity displayed in **Figures 3a to 3e** show that when the UV light is switched on, there is a decrease in the resonant frequency rapidly until it approaches a certain level where the UV light influence is much dominant than the thermal effect. As the temperature is increased, the resonant frequency is continuously decreased at a much slower rate and linearly due to thermal influence. When the UV light is switched off, the interaction between the light and ZnO thin film is instantly stopped, and the frequency is rapidly increased. However, the resonant frequency is still changed progressivly towards the original baseline due to the thermal effect where the cycling time was insufficient to reduce the temperature of the SAW device.

The results of UV sensing was performed on the ZnO/glass SAW device with various UV intensities, ranging from 0.756 to 89.5 mV/cm^2, and they are presented in **Figure 3f.** The data obtained using the ZnO/glass SAW devices show a nearly linear relationship with a UV sensitivity (*S*) value of 0.62±0.3 mV/cm^2. Upon the addition of a pristine WO_x layer onto the ZnO/glass SAW device, the UV sensitivity was observed to increase to 2.459±0.03 S. The average UV sensitivities obtained after incorporating Er-, Gd-, and Nb-doped WO_x layers onto the SAW device are 6.21±2.31, 8.60±2.1, 4.31±0.3 S respectively, as shown in **Figure 3f**. As compared to the UV sensitivity value of ZnO/glass SAW device, the improvement in UV sensitivity values were approximately 4 times, 10 times, 14 times, and 7 times for pristine WO_x layer, Er-, Gd-, and Nb-doped WO_x, respectively. **Table 2** compares properties and advantages of other doped WO_x samples which have been used to improve photocatalytic activities reported in literature. It can be implied that our obtained results for the various doped WO_x samples have shown better photocatalytic performance in terms of the measurable enhancement in UV sensitivity values when compared to ZnO/glass SAW device. For instance, our obtained results for the various doped WO_x samples have provided better enhancement in UV sensitivity of 6 times, 10 times, and 3 times for Er, Gd, and Nb doped WO_x, respectively, as compared to P-doped WO_x.

Our results demonstrate that the Gd-doped WO_x exhibits the highest sensitivity among the control group, bacause Gd doping effectively reduces the bandgap of WO_x, more than the others. Upon introduction of Gd into WO_x, a shallow donor level is formed within the bandgap, reducing the energy required for electrons transition from the valence band to the conduction band. This leads to a decrease in the bandgap, an increased electrical conductivity, and an enhanced sensitivity to ultraviolet light, thereby enhancing the photocatalytic activity. Addition to this, the fabricated sensor has a fast response time of about 5 to 10 seconds under the various UV light illumination while it takes slightly longer time (about 60 to 90 seconds) for full recovery at 365 nm.

Table 2: Properties and advantages of various metal doped WO_x for enhancing photocatalytic activity.

Metal element	Ionic radii	Features/Advantages	Reference
Phosphorus (P)	0.38 Å	• 6% P-doped WO_3 possesses best photocatalytic activity amongst other concentrations (4%, 8%, and 10%) and was four times higher as compared to pure WO_3.	[55]
Cerium (Ce)	1.01 Å	• 3% Ce-doped WO_3 possess photodegradation efficiency of 96%, better than other concentrations (1% and 5%) and pure WO_3.	[56]
Erbium (Er)	1.00 Å	• 4% Er-doped WO_3 exhibit higher photocatalytic performance than 4% La-doped WO_3 and pure WO_3	[40]
Lanthanum (La)	1.061 Å	• 4 wt.% La-doped WO_3 exhibits the photocatalytic degradation efficiency of 90% as compared to other concentrations (2 wt.%, 6 wt.%, and 8 wt.%) and pure WO_3.	[57]
Iron (Fe)	0.92 Å	• 0.5% Fe-doped WO_3 exhibits photocatalytic degradation rate of 96.8%	[58]

		as compared to other concentrations (1%, 2%, and 5%) and pure WO_3	
Gadolinium (Gd)	1.8 Å	• 2% Gd-doped WO_3 with photocatalytic degradation performance of 96% as compared to 4% La-doped WO_3, 4% Er-doped WO_3 and pure WO_3	[40]
Niobium (Nb)	0.69 Å	• Nb-doped WO_3 (atomic ratio of Nb/W = 0.03) shows effective photocatalytic activity of 85% when compared to other atomic ratios of Nb to W = 0, 0.06, 0.1, 0.15, and 0.2)	[42]

3.3. UV sensing mechansims

The primary contribution of the device to its sensitivity to UV light lies in its combination of a ZnO piezoelectric thin film and Gd-doped WO_x. ZnO is known for its wide bandgap, piezoelectric properties, and high electron mobility, while the doping of Gd in WO_x reduces the bandgap and creates shallow donor energy levels in the bandgap. When ZnO layer and Gd-doped WOx are combined, the material's electronic structure changes, causing changes in the energy required for electrons to be transported from the valence band to the conduction band. The interaction between ZnO and Gd-doped WO_x creates a more favorable matching environment for the generation of electron-hole pairs upon UV exposure, thus increasing sensitivity to UV light. When not exposed to UV light, atmospheric oxygen molecules are adsorbed onto the surface of the ZnO film and WO_x due to their inherent defects, capturing free electrons and forming negatively charged ions as indicated in the following equation. This results in a weakly conductive depleted region in the equation. [42]:

$$O_{2\,(gas)} + 2\,electron^{-} \rightarrow O^{2-}_{2\,(adsorbed)} \quad (9)$$

Upon exposure to UV light, Gd-doped WO_x acts as a trap for electrons generated by the UV radiation, enhancing the generation of electron-hole pairs, The combination of ZnO and WO_x leads to an increase in the material's conductivity, resulting in a stronger UV response. The holes recombine with electrons adsorbed by oxygen ions. This allows oxygen molecules to be

released back into the atmosphere, as indicated in the following equation. This increases the surface conductivity (σs) of the SAW sensor and reduces the depleted region [42].

$$2Hole^{+} + O^{2-}_{2\,(adsorbed)} \rightarrow O_{2(gas)} \quad (10)$$

Therefore, exposure of SAW device sensor to UV light results in an acoustic-elastic response, in which a change in the surface sheet conductivity induces a variation in the phase velocity and the amplitude of the acoustic wave. These effects are expressed with the following equations [56], [57]:

$$\frac{\Delta v}{v_0} = -\frac{k^2}{2}\frac{\sigma_s^2}{\sigma_s^2 + v_0^2 C_s^2} \quad (11)$$

$$\Delta\Gamma = \frac{k^2}{2}\frac{v_0 C_s \sigma_s}{\sigma_s^2 + v_0^2 C_s^2} \quad (12)$$

where Δv is the change of acoustic wave velocity, v_0 is the unperturbed velocity at the free surface, k^2 is the electromechanical coupling coefficient, σ_s is the surface sheet conductivity, C_s is the capacitance per unit length of the surface, $\Delta\Gamma$ is the change of signal amplitude (the insertion loss), and λ is the wavelength. Equation (11) can be rewritten with respect to the change in the resonant frequency (v = λf) as shown in Eq. (13):

$$\frac{\Delta \mathrm{f}}{f_0} = -\frac{k^2}{2}\frac{\sigma_s^2}{\sigma_s^2 + v_0^2 C_s^2} \quad (13)$$

Figure 4a shows the frequency shifts of the device at different UV intensities after irradiation at various durations (0, 1, 2, 3, 4, and 5s). The results reveal that the frequency shift of the device increases progressively with increasing UV irradiation time, which may be attributed to the thermal effect induced by the UV radiation. To substantiate this conjecture, we measured the real-time temperatures of the device surface at different light intensities. The maximum temperature increment was 3.7 °C in 5 seconds when the UV light source was used with an intensity of 100%, as shown in **Figure 4b**. The surface temperature is remarkedly increased with the UV irradiation time. Based on the measured TCF, we calculated the frequency shift induced by only thermal effect caused by UV radiation, as shown in **Figure 4c**. Notably, the frequency shift induced by the thermal effect rises from 32 kHz to 47 kHz as the UV irradiation

time is increased from 1s to 5s. To investigate the synergistic mechanism of the photoelectric and thermal effects during UV irradiation, we computed the contribution of the photoelectric effect and the thermal effect to the frequency shift at 5s, as illustrated in **Figure 4d**. Our findings reveal that the frequency shift induced by the thermal effect accounts for ~ 43% of the total frequency shift under different UV intensities [58].

Additionally, this frequency shifts are due to the combination of UV irridiation induced conductivity changing effect and thermal effect, as represented by the following equation:

$$\Delta fo = \Delta f\ (UV\ light) + \Delta f\ (Thermal\ influence) \quad (14)$$

where $\Delta f0$ is the frequency shifts, Δf is the change of frequency due to UV light and/or thermal influence.

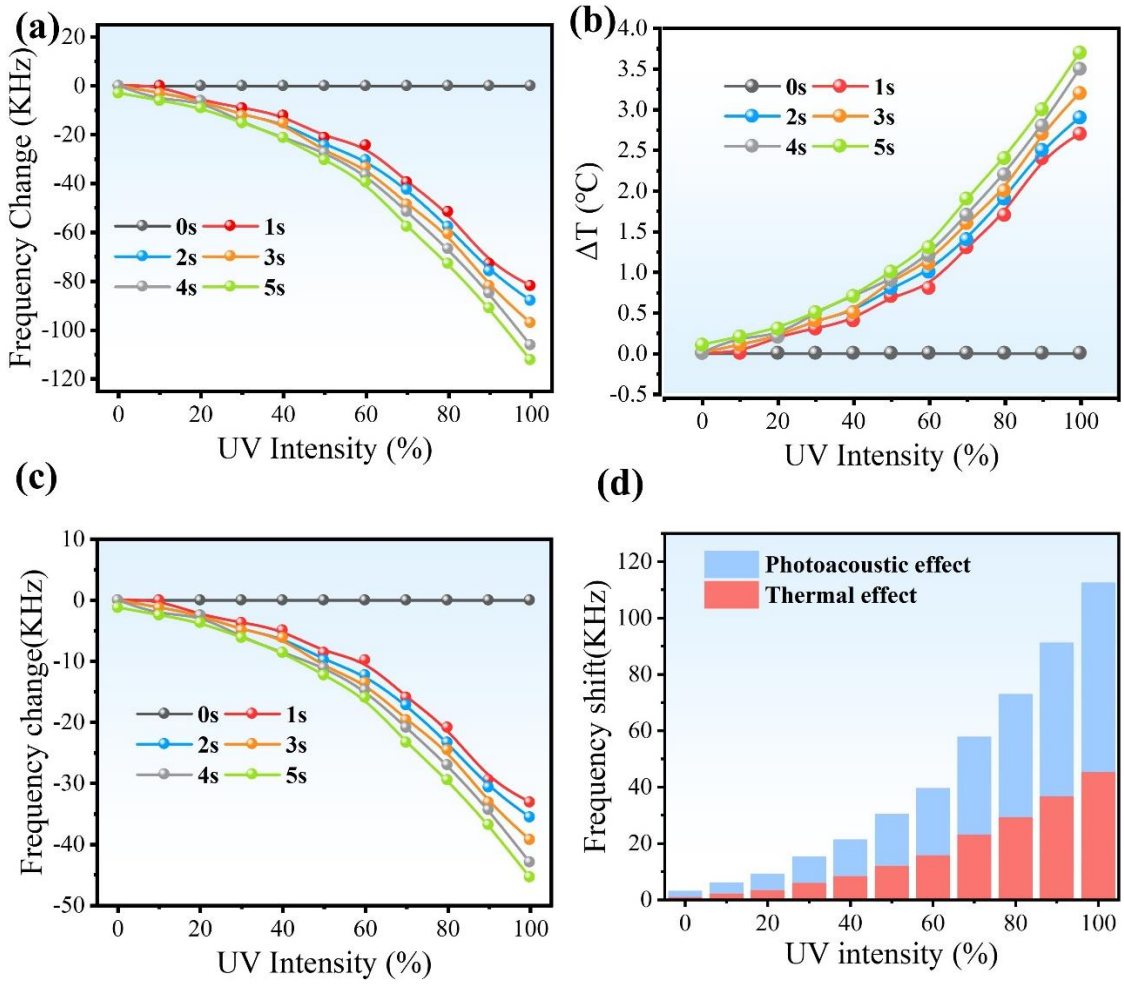

Figure 4: (a) Total frequency shift of Gd-doped WO_x devices at 0s, 1s, 2s, 3s, 4s, and 5s under different UV intensities.; (b) Variation of temperature in devices at 0s, 1s, 2s, 3s, 4s, and 5s under different UV intensities; (c) Frequency shift calculations versus UV intensities attributed

to thermal effects; (d) At 5s, the contribution ratios of photoelectric and thermal effects in devices under different light intensities.

The measured I-V characteristic curves of ZnO thin film-based SAW devices are illustrated in **Figure 5a**. The current increases exponentially from -0.5 to 5V, indicating that the film resistivity is decreased with the increase of current. However, as the UV light is switched off, the current is decreased rapidly and this further suggests a reduction in the surface sheet conductivity. Hence, the change in the surface sheet conductivity ($\Delta\sigma_s$) is governed by the following equation, assuming that the ZnO thin film has a uniform sheet thickness [59]:

$$\Delta\sigma_s = \frac{1}{\Delta R_s} = \frac{\Delta I}{\Delta V}\frac{L}{W} \tag{15}$$

where $\Delta\sigma_s$ is the change of the surface sheet conductivity, ΔR_s is the change of surface sheet resistance, ΔI is the change of the current, ΔV is the change of voltage, and L and W are the length and width of the device, respectively. The dimension value of L x W are the area occupied by the IDTs in which the UV irradiation was illuminated. The value ($\Delta I/\Delta V$) under light exposure can be obtained from the I-V curve as the current changes linearly with voltage.

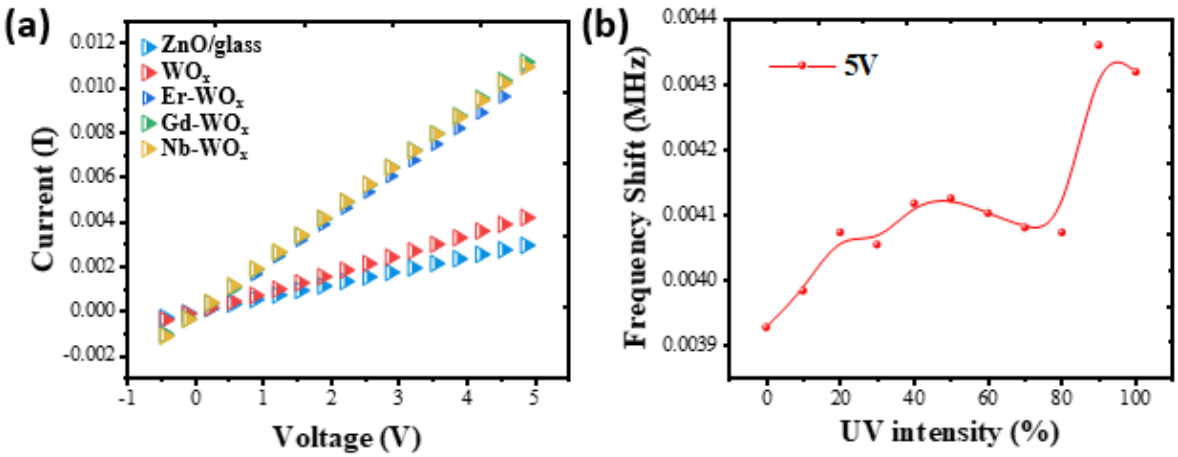

Figure 5: (a) I-V characteristics of pure ZnO/glass SAW device, pristine WO_x, Er-doped WO_x, Gd-doped WO_x, and Nb-doped WO_x; (b) Conductivity changes of Gd-doped WO_x at 5V

For the various doped WO_x coated onto ZnO/glass SAW device, when the UV light intensities was increased from 0% to 100%, there is an increment on the I-V curves. The conductance and

resistance of ZnO/glass SAW device and the different doped tungsten oxide coated devices were calculated. The original ZnO/glass device was reported to have conductance value of 0.0006 Siemens and a resistance value of 1666 ohms. The resistance values were calculated for SAW device coated with pristine WO_x, Er-, Gd-, and Nb-doped WO_x, and they are ~1111, 416, 434, and 434 ohms, respectively. Comparing the resistance values of prisine WO_x and the various doped WO_x samples, it was observed that the resistance of uncoated ZnO/glass SAW device is higher. Amongst the doped tungsten oxide elements, Er-doped WO_x device appears to have higher conductance and lower resistance values as compared to the other elements.

The changes in conductivity of Gd-doped WO_x under 5V are illustrated in **Figure 5b**. As a general trend, the change in frequency is observed to fluctuate with increasing UV intensities where the largest frequency shift is observed at UV 90% and the lowest frequency shift is observed at UV intensity of 0%. The fluctuation in frequency shifts at different UV intensities could be due to existing lingering thermal effects from the previous UV intensity testing, where it influences the sensitivity of the Gd-doped WO_x.

The I-V characteristic curves demonstrate that when UV light intensity is increased, the surface sheet conductivity of ZnO thin fim is increased as well. The frequency shifts as a result of conductivity changes, and the resonant frequency decreases linearly with increasing UV light intensity. When a high UV intensity is utilised, thermal effect shows a considerable impact on variations in the resonant frequency; however, when a low UV intensity was utilised, it has little impact on the resonant frequency.

Based on the results obtained, the UV sensing mechanism enhanced by the dopants in the proposed UV sensor can be further discussed. Through the band gap engineering and enhanced absorption of UV, the incorporation of dopants Gd into the WOx matrix plays a crucial role for the enhancement in UV sensing performance. Doping introduces impurity levels within the bandgap, reducing the effective band gap of the material. This reduction in the band gap results in the improved light absorption across a broader spectral range, including both UV and visible regions. From this, the doped WOx becomes more responsive to UV irradiation, increasing the generation of electron-hole pairs upon photon absorption. Furthermore, the generation of increased amount of charge carriers where the creation of shallow donor energy levels thorugh doping Gd provides additional pathways for electron-hole pair generation. When UV photons are absorbed, they generate electron-hole pairs in the doped WO_x material. These additional

charge carriers contribute to an increased photoresponse due to their enhanced availability for charge transport.

Doping with elements such as Gd can modify the electronic structures and carrier mobilities of the materials. These modifications lead to an increase in the electrical conductivity. The presence of additional charge carriers and the modified charge transport properties contribute to a higher sensitivity to UV-induced changes in conductivity. Moreover, doping-induced energy levels act as charge traps, enhancing the separation of photogenerated electron-hole pairs. In the presense of these traps, charge carriers are less likely to recombine, leading to a higher concentration of free charge carriers available for conduction. This efficient charge separation and recombination suppression further amplify the sensor's response to UV radiation. In addition, dopants such as Gd can introduce oxygen vacancies in the WO_x lattice. These oxygen vacancies serve as active sites for charge carrier generation and transport. The increased concentration of oxygen vancacies enhances the material's overall conductivity, contributing to a more pronounced change in conductivity when exposed to UV light.

In summary, the incorporation of dopants such as Gd into the WO_x matrix leads to a multitude of effects that collectively enhance the UV sensing performance. These effects include modified band gap, increased charge carrier generation, enhanced conductivity, efficient charge separation, and recombination suppression.

4.0 Conclusions

WO_x powder samples, modified with metal elements, were fabricated to enhance photocatalytic performance. This was achieved through the concept of doping and band gap engineering via a one-step solvothermal method. Our studies reveal that Gd-doped WO_x coated SAW dveice exhibits superior performance with 14 times enhancement in UV sensitivity when compared to uncoated ZnO/glass SAW device, which was characterized by a lower band gap and heightened sensitivity. The increased sensitivity can be attributed to the unique 4f electrons present in Gd. This, in turn, alters the electron energy band structure of WO_x and the large atomic radius of Gd impacts the structural and band gap configurations within WO_x. Furthermore, our analysis of the UV sensing mechanism on ZnO/glass surface acoustic wave devices coated with Gd-doped WO_x reveals that frequency shifts are primarily driven by changes in conductivity and thermal effects induced by ultraviolet radiation.

Acknowledgement

This work was financially supported by the UK Engineering and Physical Sciences Research Council (EPSRC) under grant EP/P018998/1, Newton Mobility Grant (IE161019) through Royal Society, the National Natural Science Foundation of China (11504291,52075162, 12104320), Research Project in Fundamental and Application Fields of Guangdong Province (2020A1515110561), Shenzhen Science & Technology Project (RCBS20200714114918249), the Innovation Leading Program of New and High-tech Industry of Hunan Province (2020GK2015), the Natural Science Foundation of Hunan Province (2021JJ20018), and the Natural Science Foundation of Changsha (kq2007026).

References

[1] M. Tayyib, J. O. Odden, and T. O. Saetre, "UV-induced Degradation Study of Multicrystalline Silicon Solar Cells Made from Different Silicon Materials," *Energy Procedia*, vol. 38, pp. 626–635, Jan. 2013, doi: 10.1016/J.EGYPRO.2013.07.326.

[2] D. H. Sliney and B. E. Stuck, "A Need to Revise Human Exposure Limits for Ultraviolet UV-C Radiation†," *Photochem. Photobiol.*, vol. 97, no. 3, pp. 485–492, May 2021, doi: 10.1111/PHP.13402.

[3] A. H, M. M. El-Tonsy, and A. A. jalil. A. Shumis, "Degradation of glass polymers due to successive exposure to acid rain and UV radiation," *J. Adv. Phys.*, vol. 11, no. 2, pp. 2979–2989, Nov. 2015, doi: 10.24297/JAP.V11I2.530.

[4] H. Shamachurn and T. Betts, "Experimental Study of the Degradation of Silicon Photovoltaic Devices under Ultraviolet Radiation Exposure," *J. Sol. Energy*, vol. 2016, pp. 1–9, Jul. 2016, doi: 10.1155/2016/2473245.

[5] W. Zou, M. Sastry, J. J. Gooding, R. Ramanathan, and V. Bansal, "Recent Advances and a Roadmap to Wearable UV Sensor Technologies," *Adv. Mater. Technol.*, vol. 5, no. 4, Apr. 2020, doi: 10.1002/ADMT.201901036.

[6] J. D'Orazio, S. Jarrett, A. Amaro-Ortiz, and T. Scott, "UV Radiation and the Skin," *Int. J. Mol. Sci.*, vol. 14, no. 6, p. 12222, 2013, doi: 10.3390/IJMS140612222.

[7] S. hao Deng, H. Lu, and D. Y. Li, "Influence of UV light irradiation on the corrosion behavior of electrodeposited Ni and Cu nanocrystalline foils," *Sci. Rep.*, vol. 10, no. 1, Dec. 2020, doi: 10.1038/S41598-020-59420-6.

[8] A. Sinha *et al.*, "UV-Induced Degradation of High-Efficiency Solar Cells with Different Architectures," *Conf. Rec. IEEE Photovolt. Spec. Conf.*, vol. 2020-June, pp. 1990–1991, Jun. 2020, doi: 10.1109/PVSC45281.2020.9300993.

[9] S. W. Lee *et al.*, "UV Degradation and Recovery of Perovskite Solar Cells," *Sci. Reports 2016 61*, vol. 6, no. 1, pp. 1–10, Dec. 2016, doi: 10.1038/srep38150.

[10] A. Kumar *et al.*, "ZnS microspheres-based photoconductor for UV light-sensing

applications," *Chem. Phys. Lett.*, vol. 763, p. 138162, Jan. 2021, doi: 10.1016/J.CPLETT.2020.138162.

[11] A. Kumar *et al.*, "Highly responsive and low-cost ultraviolet sensor based on ZnS/p-Si heterojunction grown by chemical bath deposition," *Sensors Actuators A Phys.*, vol. 331, p. 112988, Nov. 2021, doi: 10.1016/J.SNA.2021.112988.

[12] A. Kumar *et al.*, "Fabrication of low-cost and fast-response visible photodetector based on ZnS:Mn/p-Si heterojunction," *Mater. Sci. Semicond. Process.*, vol. 155, p. 107226, Mar. 2023, doi: 10.1016/J.MSSP.2022.107226.

[13] X. Sheng *et al.*, "Silicon-Based Visible-Blind Ultraviolet Detection and Imaging Using Down-Shifting Luminophores," *Adv. Opt. Mater.*, vol. 2, no. 4, pp. 314–319, Apr. 2014, doi: 10.1002/ADOM.201300475.

[14] N. Aggarwal *et al.*, "A Highly Responsive Self-Driven UV Photodetector Using GaN Nanoflowers," *Adv. Electron. Mater.*, vol. 3, no. 5, p. 1700036, May 2017, doi: 10.1002/AELM.201700036.

[15] Z. Zhan, L. Zheng, Y. Pan, G. Sun, and L. Li, "Self-powered, visible-light photodetector based on thermally reduced graphene oxide–ZnO (rGO–ZnO) hybrid nanostructure," *J. Mater. Chem.*, vol. 22, no. 6, pp. 2589–2595, Jan. 2012, doi: 10.1039/C1JM13920G.

[16] H.-F. Pang *et al.*, "Love mode surface acoustic wave ultraviolet sensor using ZnO films deposited on 36 • Y-cut LiTaO 3," *Sensors Actuators A. Phys.*, vol. 193, pp. 87–94, 2013, doi: 10.1016/j.sna.2013.01.016.

[17] J. Zhou *et al.*, "Transparent surface acoustic wave devices on Zno/Glass using Al-doped Zno as the electrode," *IEEE Electron Device Lett.*, vol. 34, no. 10, pp. 1319–1321, 2013, doi: 10.1109/LED.2013.2276618.

[18] X. Tao *et al.*, "Three-Dimensional Tetrapodal ZnO Microstructured Network Based Flexible Surface Acoustic Wave Device for Ultraviolet and Respiration Monitoring Applications," *ACS Appl. Nano Mater.*, vol. 3, no. 2, pp. 1468–1478, Feb. 2020, doi: 10.1021/ACSANM.9B02300.

[19] Y. Zhang *et al.*, "Surface acoustic wave-based ultraviolet photodetectors: a review," *Sci. Bull.*, vol. 65, no. 7, pp. 587–600, Apr. 2020, doi: 10.1016/J.SCIB.2019.12.001.

[20] X. L. He *et al.*, "High performance dual-wave mode flexible surface acoustic wave resonators for UV light sensing," *J. Micromechanics Microengineering*, vol. 24, no. 5, 2014, doi: 10.1088/0960-1317/24/5/055014.

[21] C. Li *et al.*, "A high performance surface acoustic wave visible light sensor using novel materials: Bi2S3 nanobelts," *RSC Adv.*, vol. 10, no. 15, p. 8936, Feb. 2020, doi: 10.1039/C9RA08848B.

[22] W. S. Wang, C. J. Tsai, and C. C. Ma, "Qualitative and quantitative analysis of surface-acoustic-wave-based ultraviolet photodetectors," *J. Appl. Phys.*, vol. 114, no. 6, Aug. 2013, doi: 10.1063/1.4817868.

[23] D. Mandal and S. Banerjee, "Surface Acoustic Wave (SAW) Sensors: Physics, Materials, and Applications," 2022.

[24] Y. Q. Fu *et al.*, "Advances in piezoelectric thin films for acoustic biosensors,

acoustofluidics and lab-on-chip applications," *Prog. Mater. Sci.*, vol. 89, pp. 31–91, Aug. 2017, doi: 10.1016/J.PMATSCI.2017.04.006.

[25] S. Kumar *et al.*, "Effect of silica on the ZnS nanoparticles for stable and sustainable antibacterial application," *Int. J. Appl. Ceram. Technol.*, vol. 16, no. 2, pp. 531–540, Mar. 2019, doi: 10.1111/IJAC.13145.

[26] S. A. Hasan, H. Torun, D. Gibson, Q. Wu, M. D. Cooke, and Y. Fu, "Flexible UV sensor based on nanostructured ZnO thin film SAW device," *2019 IEEE Jordan Int. Jt. Conf. Electr. Eng. Inf. Technol. JEEIT 2019 - Proc.*, pp. 85–90, May 2019, doi: 10.1109/JEEIT.2019.8717373.

[27] M. F. Khan *et al.*, "Flower-shaped ZnO nanoparticles synthesized by a novel approach at near-room temperatures with antibacterial and antifungal properties," *Int. J. Nanomedicine*, vol. 9, no. 1, p. 853, Feb. 2014, doi: 10.2147/IJN.S47351.

[28] Y. J. Lu, Z. F. Shi, C. X. Shan, and D. Z. Shen, "ZnO nanostructures and lasers," *Nanoscale Semicond. Lasers*, pp. 75–108, Jan. 2019, doi: 10.1016/B978-0-12-814162-5.00004-2.

[29] H. Quan, Y. Gao, and W. Wang, "Tungsten oxide-based visible light-driven photocatalysts: crystal and electronic structures and strategies for photocatalytic efficiency enhancement," *Inorg. Chem. Front.*, vol. 7, no. 4, pp. 817–838, Feb. 2020, doi: 10.1039/C9QI01516G.

[30] N. Zhang *et al.*, "Monoclinic Tungsten Oxide with {100} Facet Orientation and Tuned Electronic Band Structure for Enhanced Photocatalytic Oxidations," *ACS Appl. Mater. Interfaces*, vol. 8, no. 16, pp. 10367–10374, Apr. 2016, doi: 10.1021/ACSAMI.6B02275/SUPPL_FILE/AM6B02275_SI_001.PDF.

[31] C. M. Wu, S. Naseem, M. H. Chou, J. H. Wang, and Y. Q. Jian, "Recent advances in tungsten-oxide-based materials and their applications," *Front. Mater.*, vol. 6, p. 49, Mar. 2019, doi: 10.3389/FMATS.2019.00049/BIBTEX.

[32] X. Zhang, S. He, and S. P. Jiang, "WOx/g-C3N4 layered heterostructures with controlled crystallinity towards superior photocatalytic degradation and H2 generation," *Carbon N. Y.*, vol. 156, pp. 488–498, Jan. 2020, doi: 10.1016/J.CARBON.2019.09.083.

[33] X. Zhang, K. Matras-Postolek, P. Yang, and S. Ping Jiang, "Z-scheme WOx/Cu-g-C3N4 heterojunction nanoarchitectonics with promoted charge separation and transfer towards efficient full solar-spectrum photocatalysis," *J. Colloid Interface Sci.*, vol. 636, pp. 646–656, Apr. 2023, doi: 10.1016/J.JCIS.2023.01.052.

[34] H. Kim, R. O. Bonsu, C. Odonohue, R. Y. Korotkov, L. McElwee-White, and T. J. Anderson, "Aerosol-assisted chemical vapor deposition of tungsten oxide films and nanorods from oxo tungsten(VI) fluoroalkoxide precursors," *ACS Appl. Mater. Interfaces*, vol. 7, no. 4, pp. 2660–2667, Feb. 2015, doi: 10.1021/AM507706E.

[35] W. Raza, S. M. Faisal, M. Owais, D. Bahnemann, and M. Muneer, "Facile fabrication of highly efficient modified ZnO photocatalyst with enhanced photocatalytic, antibacterial and anticancer activity," *RSC Adv.*, vol. 6, no. 82, pp. 78335–78350, 2016, doi: 10.1039/c6ra06774c.

[36] K. Ariga, "Materials Nanoarchitectonics: Collaboration between Chem, Nano and

Mat," *ChemNanoMat*, Jul. 2023, doi: 10.1002/CNMA.202300120.

[37] A. H. Y. Hendi *et al.*, "Modulation of the band gap of tungsten oxide thin films through mixing with cadmium telluride towards photovoltaic applications," *Mater. Res. Bull.*, vol. 87, pp. 148–154, Mar. 2017, doi: 10.1016/J.MATERRESBULL.2016.11.032.

[38] R. Jolly Bose, R. Vinod Kumar, S. K. Sudheer, V. R. Reddy, V. Ganesan, and V. P. Mahadevan Pillai, "Effect of silver incorporation in phase formation and band gap tuning of tungsten oxide thin films," *J. Appl. Phys.*, vol. 112, no. 11, p. 114311, Dec. 2012, doi: 10.1063/1.4768206.

[39] X. Sun, Z. Liu, and H. Cao, "Electrochromic properties of N-doped tungsten oxide thin films prepared by reactive DC-pulsed sputtering," *Thin Solid Films*, vol. 519, no. 10, pp. 3032–3036, Mar. 2011, doi: 10.1016/J.TSF.2010.12.017.

[40] A. Gupta, S. Rajawat, and M. M. Malik, "Study of UV-sensitive Ag doped WO3 prepared using ultra-sonification," *Optik (Stuttg).*, vol. 242, p. 167266, Sep. 2021, doi: 10.1016/J.IJLEO.2021.167266.

[41] M. Bilal Tahir and M. Sagir, "Carbon nanodots and rare metals (RM = La, Gd, Er) doped tungsten oxide nanostructures for photocatalytic dyes degradation and hydrogen production," *Sep. Purif. Technol.*, vol. 209, pp. 94–102, Jan. 2019, doi: 10.1016/J.SEPPUR.2018.07.029.

[42] W. Q. Wang, Z. J. Yao, X. L. Wang, X. H. Xia, C. D. Gu, and J. P. Tu, "Niobium doped tungsten oxide mesoporous film with enhanced electrochromic and electrochemical energy storage properties," *J. Colloid Interface Sci.*, vol. 535, pp. 300–307, Feb. 2019, doi: 10.1016/J.JCIS.2018.10.006.

[43] W. Mu *et al.*, "Characterizations of Nb-doped WO3 nanomaterials and their enhanced photocatalytic performance," *RSC Adv.*, vol. 4, no. 68, pp. 36064–36070, 2014, doi: 10.1039/c4ra04080e.

[44] E. Cerrato, E. Gaggero, P. Calza, and M. C. Paganini, "The role of Cerium, Europium and Erbium doped TiO2 photocatalysts in water treatment: A mini-review," *Chem. Eng. J. Adv.*, vol. 10, p. 100268, May 2022, doi: 10.1016/J.CEJA.2022.100268.

[45] B. Ortega-Berlanga, L. Betancourt-Mendiola, C. Del Angel-Olarte, L. Hernández-Adame, S. Rosales-Mendoza, and G. Palestino, "An overview of gadolinium-based oxide and oxysulfide particles: Synthesis, properties, and biomedical applications," *Crystals*, vol. 11, no. 9, pp. 1–34, 2021, doi: 10.3390/cryst11091094.

[46] C. del Angel-Olarte, L. Hernández-Adame, A. Mendez-Blas, and G. Palestino, "Eu3+/Yb3+ co-doped gadolinium oxysulfide upconverting nanorods: Morphological, physicochemical and optical evaluation," *J. Alloys Compd.*, vol. 787, pp. 1032–1043, May 2019, doi: 10.1016/J.JALLCOM.2019.02.113.

[47] S. L. Woon, C. H. Pua, H. S. Lin, and F. A. Rahman, "Application of Erbium-Doped Fibre Laser Dynamics in Pipeline Leak Detection and Location Estimation," *2018 IEEE 7th Int. Conf. Photonics, ICP 2018*, Nov. 2018, doi: 10.1109/ICP.2018.8533164.

[48] H. Ong *et al.*, "ZnO/glass thin film surface acoustic waves for efficient digital acoustofluidics and active surface cleaning," *Mater. Chem. Phys.*, vol. 287, p. 126290, Aug. 2022, doi: 10.1016/J.MATCHEMPHYS.2022.126290.

[49] R. Tao *et al.*, "Bimorph material/structure designs for high sensitivity flexible surface acoustic wave temperature sensors," *Sci. Rep.*, vol. 8, no. 1, Dec. 2018, doi: 10.1038/S41598-018-27324-1.

[50] M. Morsy, I. Gomaa, M. M. Mokhtar, H. ElHaes, and M. Ibrahim, "Design and implementation of humidity sensor based on carbon nitride modified with graphene quantum dots," *Sci. Reports 2023 131*, vol. 13, no. 1, pp. 1–18, Feb. 2023, doi: 10.1038/s41598-023-29960-8.

[51] A. I. Madbouly, W. S. Hassanien, and M. Morsy, "Tailoring the polyurethane foam/rGO/BaTiO3 pressure sensor for human activities," *Diam. Relat. Mater.*, vol. 136, p. 109940, Jun. 2023, doi: 10.1016/J.DIAMOND.2023.109940.

[52] A. Singh, D. Kumar, P. K. Khanna, M. Kumar, and B. Prasad, "Post annealing effect on structural and optical properties of ZnO thin films derived by sol-gel route," *J. Mater. Sci. Mater. Electron.*, vol. 24, no. 11, pp. 4607–4613, Nov. 2013, doi: 10.1007/S10854-013-1451-4/TABLES/2.

[53] Y. Wang *et al.*, "Visualizing Light-Induced Microstrain and Phase Transition in Lead-Free Perovskites Using Time-Resolved X-Ray Diffraction," *J. Am. Chem. Soc.*, vol. 144, no. 12, pp. 5335–5341, 2022, doi: 10.1021/jacs.1c11747.

[54] H. F. Pang *et al.*, "Characterization of the surface acoustic wave devices based on ZnO/nanocrystalline diamond structures," *Phys. status solidi*, vol. 210, no. 8, pp. 1575–1583, Aug. 2013, doi: 10.1002/PSSA.201228631.

[55] H. Zhang and H. Wang, "Investigation of Surface Acoustic Wave Propagation Characteristics in New Multilayer Structure: SiO2/IDT/LiNbO3/Diamond/Si," *Micromachines 2021, Vol. 12, Page 1286*, vol. 12, no. 11, p. 1286, Oct. 2021, doi: 10.3390/MI12111286.

[56] V. Chivukula, D. Ciplys, M. Shur, and P. Dutta, "ZnO nanoparticle surface acoustic wave UV sensor," *Appl. Phys. Lett.*, vol. 96, no. 23, 2010, doi: 10.1063/1.3447932.

[57] L. Shi and S. Nihtianov, "Comparative study of silicon-based ultraviolet photodetectors," *IEEE Sens. J.*, vol. 12, no. 7, pp. 2453–2459, 2012, doi: 10.1109/JSEN.2012.2192103.

[58] Y. Zou, Y. Zhang, Y. Hu, and H. Gu, "Ultraviolet Detectors Based on Wide Bandgap Semiconductor Nanowire: A Review," *Sensors 2018, Vol. 18, Page 2072*, vol. 18, no. 7, p. 2072, Jun. 2018, doi: 10.3390/S18072072.

[59] Y. Y. Chiu, W. Y. Lin, H. Y. Wang, S. Bin Huang, and M. H. Wu, "Development of a piezoelectric polyvinylidene fluoride (PVDF) polymer-based sensor patch for simultaneous heartbeat and respiration monitoring," *Sensors Actuators, A Phys.*, vol. 189, pp. 328–334, 2013, doi: 10.1016/J.SNA.2012.10.021.